



Attractor selection in nonlinear oscillators by temporary dual-frequency driving

Péter Krähling · Joshua Steyer · Ulrich Parlitz  · Ferenc Hegedűs

Received: 22 December 2022 / Accepted: 20 August 2023 / Published online: 12 September 2023
© The Author(s) 2023

Abstract This paper presents a control technique capable of driving a harmonically driven nonlinear system between two distinct periodic orbits. A vital component of the method is a temporary dual-frequency driving with tunable driving amplitudes. Theoretical considerations revealed two necessary conditions: one for the frequency ratio of the dual-frequency driving and another one for torsion numbers of the two orbits connected by bifurcation curves in the extended dual-frequency driving parameter space. Although the initial

and the final states of the control strategy are single-frequency driven systems with distinct parameter sets (frequencies and driving amplitudes), control of multistability is also possible via additional parameter tuning. The technique is demonstrated on the symmetric Duffing oscillator and the asymmetric Toda oscillator.

Keywords Dual-frequency driving · Bifurcation structure · Nonlinear oscillators · Attractor selection · Control of multistability

Supplementary Information The online version contains supplementary material available at <https://doi.org/10.1007/s11071-023-08855-3>.

P. Krähling · F. Hegedűs
Department of Hydrodynamic Systems, Faculty of Mechanical Engineering, Budapest University of Technology and Economics, Budapest, Hungary
e-mail: pkrähling@hds.bme.hu

F. Hegedűs
e-mail: fhgedus@hds.bme.hu

J. Steyer · U. Parlitz
Research Group Biomedical Physics, Max Planck Institute for Dynamics and Self-Organization, Göttingen, Germany
e-mail: joshua.steyer@kit.edu

J. Steyer · U. Parlitz (✉)
Institute for the Dynamics of Complex Systems, Georg-August-Universität Göttingen, Göttingen, Germany
e-mail: ulrich.parlitz@ds.mpg.de

J. Steyer
Institute of Biomedical Engineering, Karlsruhe Institute of Technology, Karlsruhe, Germany

1 Introduction

Since the discovery of the chaotic Lorenz attractor [1] in 1963, six decades have passed, and still, a significant amount of studies are published yearly to understand the complex nature and bifurcation patterns of various nonlinear systems. The organisation of fixed points, periodic orbits, quasiperiodic and chaotic solutions in multidimensional parameter spaces is a primary focus in many scientific disciplines from biology [2–6], chemistry [7–10], fluid dynamics [11–13], climate science [14–16], electronics [17, 18], plasma [19, 20] and laser physics [21–24] to classic engineering [25–28], economy [29–31] or even psychology [32].

What makes nonlinear systems so fascinating? The reason is their highly complex dynamics. The organisation of periodic orbits, often interrupted by chaotic domains, can be so intricate that a significant number of studies are published annually to better understand the

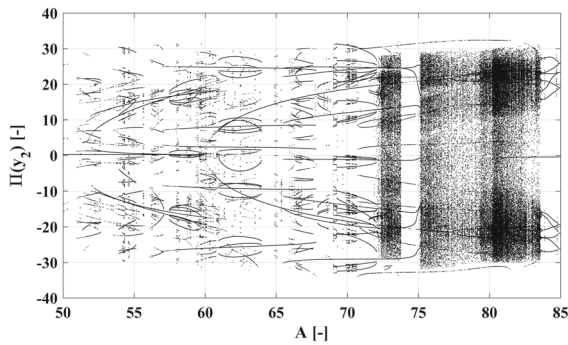


Fig. 1 Example of a one-dimensional orbit diagram, where the second component of the Poincaré section is plotted vs. the driving amplitude. The model equation is a single-frequency driven Duffing oscillator, see Sect. 4

evolution of the systems as a function of one or more control parameters. The primary goal, usually, is to describe the organisation of periodic and chaotic attractors. Although various universal bifurcation patterns have already been found, such as Feigenbaum period-doubling cascades [33–36], organisation of bifurcation structures as a Farey-tree [37–42] or shrimp-shaped isoperiodic structures [43–49], the complete picture, even in the case of simple nonlinear systems like the Duffing oscillator [50–53], the Toda oscillator [54–56] or the Lorenz system [57,58], is not yet fully explored.

Mapping and describing the structure of attractors is usually a real challenge, even in the case of a single control parameter. For demonstration purposes, a one-dimensional orbit diagram is plotted in Fig. 1 employing the single-frequency driven Duffing oscillator; for the details of the model, the reader is referred to Sect. 4. In this diagram, the second component of the Poincaré section is plotted as a function of the driving amplitude A at a fixed angular frequency value ($f = 3$) and damping rate ($d = 0.02$). In the control parameter range from approximately $A = 50$ – 72 , a complex structure of periodic attractors (up to period-32) occurs. In the overlapping regions of such orbits, there are multistable states. The scattered points at high amplitude values suggest chaotic dynamics.

The complex dynamics shown in Fig. 1 has severe consequences for applications. First, in the case of multistability, depending on the extent of the basin of attraction of a stable state, any small perturbation can lead to significantly different dynamics. Second, even if the precise adjustment of the parameter set is not mandatory, one might encounter an overwhelm-

ingly large number of stable states for a possible operation in a given parameter domain. In both situations, a technique capable of driving a nonlinear system to a selected attractor is useful to eliminate unpredictable or undesirable behaviour.

Mastering multistability is an important task in nonlinear dynamics [59], where a system is controlled to a selected attractor while keeping its parameter sets unaltered or only slightly perturbed. To achieve this goal, three main control strategies are widespread in the literature: (i) non-feedback techniques, (ii) feedback techniques and (iii) stochastic control. Non-feedback techniques are simple and easy to use. In this case, kicking the system to another stable state [60–63] or to annihilate attractors by periodic perturbation (modulation) of a parameter or a state variable [64–67] is the primary tool. Their disadvantage is that direct attractor selection is not possible. With feedback control strategies, attractor selection is possible. However, information is necessary about the state (for some techniques, the Jacobian as well) of the solution [68–71]. Therefore, feedback control techniques are unsuitable for problems, where the required data cannot be retrieved easily [72,73]. Stochastic control operates with attractor annihilation by external noise [74–76]. Since attractors are destructed in the order of the size of their basin, the control over the direct attractor selection is again lost.

The control technique proposed in this paper enables attractor selection without applying feedback to the system. However, knowledge about details of the bifurcation structure are necessary, and the parameters cannot be kept constant. Therefore, we categorise it as a feedforward method. It works for periodic orbits of harmonically driven nonlinear systems by means of a temporary dual-frequency driving. Control of multistability is possible with an additional adjustment process: after the selection of the desired attractor (periodic orbit), the parameters have to be tuned back to their original value.

This technique has already been demonstrated in our previous study [77] between a period-2 orbit and a period-3 orbit of a model describing the radial pulsation of a single spherical bubble relevant in the scientific field of sonochemistry [78–82]. In the follow-up paper [83], the attractor targeting was applied to a much larger set of periodic orbits to demonstrate that it is not an accidental case between the period-2 and period-3 attractors. These previous studies were based on a *trial-and-error approach*. Thus, one of the main

aims of the present study is to provide a more *systematic approach to identify possible transitions* between periodic orbits. For the presented control scenario, two necessary conditions are identified: a condition for the frequency ratio; and a condition for the torsion number that describes the local flow around the periodic orbits. In order to prove that the technique is not only applicable to the bubble oscillator investigated in previous publications [77,83], two other oscillators are employed here: the asymmetric Toda oscillator [84,85] and the symmetric Duffing [86] oscillator.

2 Criteria for attractor selection

In this section, we introduce general criteria for attractor selection by dual-frequency driving. The general form of the model equations is written as

$$\dot{y}_1 = F_1(y_1, y_2), \tag{1}$$

$$\dot{y}_2 = F_2(y_1, y_2) + f_D(t), \tag{2}$$

where F_1 and F_2 represent a second-order nonlinear system. Function f_D is defined as

$$f_D(t) = A \sin(ft) \tag{3}$$

for single-frequency driving, and

$$f_D(t) = A_1 \sin(f_1t) + A_2 \sin(f_2t) \tag{4}$$

for the general dual-frequency driven cases. The driving angular frequencies are f , f_1 and f_2 ; their corresponding amplitudes are A , A_1 and A_2 , respectively. From now on, angular frequency is referred to as frequency for simplicity.

Suppose that in the single-frequency driven case, two domains of periodic orbits exist in the parameter plane $A-f$. Figure 2a shows a schematic drawing of a possible configuration with period numbers p_1 (domain enclosed by the blue curves) and p_2 (domain enclosed by the red curves). Note that the values of p_1 and p_2 are integer multiples of the period of the driving $T = 2\pi/f$. Furthermore, let us assume that by continuous tuning of the amplitude A and frequency f within a domain, the system exhibits a continuous change in its dynamics with a constant period number (p_1 or p_2).

Figure 2b shows a one-dimensional section, where an arbitrarily selected component of the Poincaré map

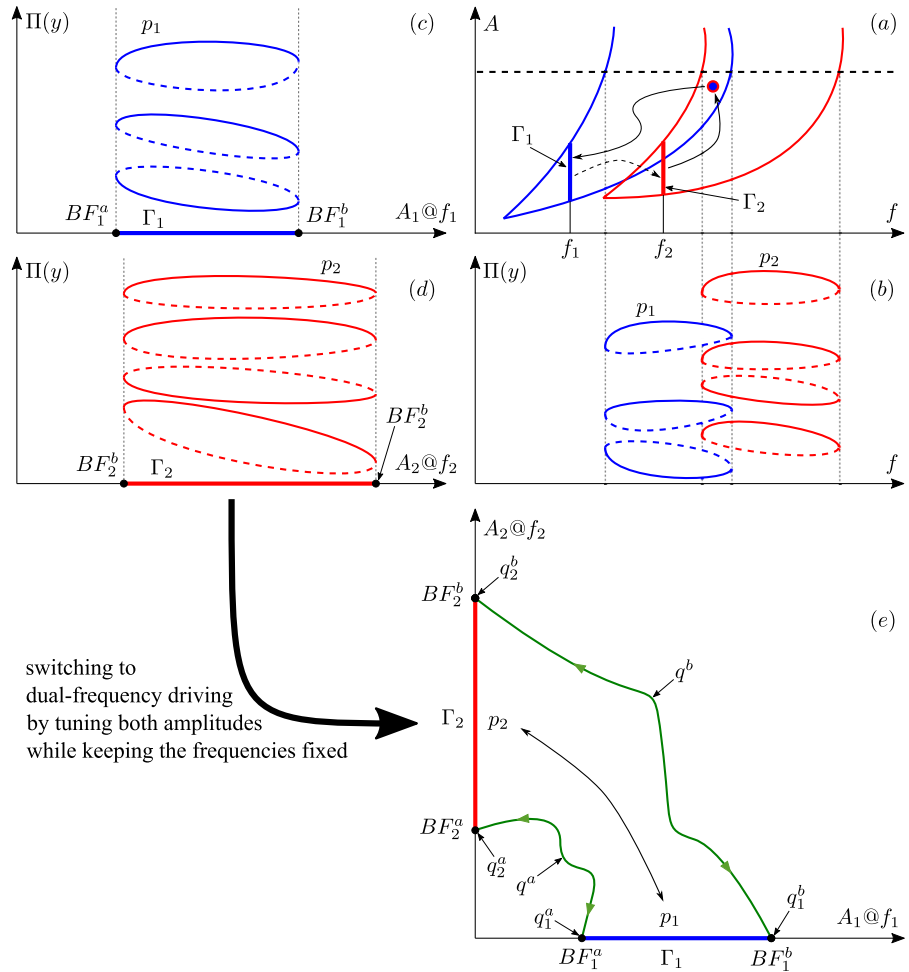
is plotted as a function of the frequency at a fixed driving amplitude. The solid and the dashed curves are stable and unstable orbits, respectively. Note that the two kinds of periodic orbits (blue and red) are not connected. Additionally, there may be many other stable states the system can converge to in case of tuning A and/or f . The number of branches presented in Fig. 2b is only for demonstration purposes; there are no restrictions for the values of p_1 and p_2 . Therefore, there is no trivial strategy to drive the system from one type of orbit to the other (e.g. by simply extending the parameter space [87]) since no bifurcation exists that connect branches of orbits having arbitrary period numbers.

Consider two frequency values f_1 and f_2 along the axis f in Fig. 2a. A pair of one-dimensional sections are presented in Fig. 2c-d, where again an arbitrarily selected component of the Poincaré map is plotted as a function of the driving amplitude at the corresponding fixed frequencies. The number of the branches and their colour code are the same as in the case of Fig. 2b. Suppose these curves are bounded by bifurcation points denoted by BF_1^a , BF_1^b , BF_2^a and BF_2^b . Their projections to the $A-f$ parameter plane are indicated by blue Γ_1 and red Γ_2 lines; see the vertical lines in Fig. 2a, and the horizontal lines on the axis of Fig. 2c-e.

Our attractor selection technique tries to drive the system from Γ_1 to Γ_2 (or vice versa) via the continuous tuning of the dual-frequency driving amplitudes A_1 and A_2 by employing dual-frequency driving with the frequency values of f_1 and f_2 . In the parameter plane of the driving amplitudes A_1-A_2 , Γ_1 and Γ_2 lie along the coordinate axis representing special, single-frequency driven cases of the general dual-frequency driving, see Fig. 2e. Therefore, the dual-frequency driving is temporary; the initial and the final states are always driven by a single frequency ($f = f_1$ or $f = f_2$).

As long as the governing equations are smooth in terms of state variables and parameters (our case), the solution has a smooth dependence on the initial conditions and parameters. In this case, showing that the pairs of bifurcation points $BF_1^a-BF_2^a$ and $BF_1^b-BF_2^b$ are connected, highlighted by the green curves in Fig. 2e, proves the existence of a *control surface* that connects the curves Γ_1 and Γ_2 and exists at least in the vicinity of the blue, red and green curves. Its projection to the A_1-A_2 plane, the *control area*, is bounded by the red, blue and green curves. There are two necessary conditions for the existence of the configuration depicted in Fig. 2e, which are discussed in Sects. 2.1 and 2.2. It is

Fig. 2 Schematic drawings to demonstrate the attractor selection process. **a** domains of period orbits of single-frequency driven system. The blue and red domains correspond to period numbers p_1 and p_2 , respectively. **b** stable and unstable periodic orbits represented by one-dimensional curves of an arbitrarily selected component of the Poincaré map $\Pi(y)$ as a function of the driving frequency f at a fixed amplitude A . **c–d** one-dimensional curves of an component of the Poincaré map $\Pi(y)$ as a function of the driving amplitude A at fixed frequencies f_1 or f_2 . **e** representation of a control area bounded by the green, blue and red curves. Notations BF and q mean bifurcation points and torsion numbers, respectively. The necessary conditions for the attractor selection process in terms of the period and the torsion numbers are discussed in Sects. 2.1 and 2.2



switching to dual-frequency driving by tuning both amplitudes while keeping the frequencies fixed

to be stressed that a suitable control surface can have a more complex topology that cannot be described with a simple configuration shown in Fig. 2e. Although an example is presented in Sect. 4.2, the detailed discussion of these situations is out of the scope of the present study.

If the attractor selection technique works, control of multistability is also possible, however, with additional control processes. The workflow is highlighted by the solid and dashed thin line arrows in Fig. 2a. Suppose that the blue/red dots define the desired parameter combination, and the system initially resides on the blue orbit having period number p_1 . First, the system has to be driven from the blue dot to the blue vertical thick line via tuning the driving parameters A and f of the single frequency driving. Next, apply the above-described attractor selection technique to arrive at the red curve having period number p_2 . A dashed line arrow marks

this process as it takes place in the $A_1 - A_2$ plane instead of the $A - f$ parameter space. Finally, drive the system back to the initial parameter combination via tuning A and f .

2.1 Period number compatibility

Although the period number p_1 in terms of single-frequency driving with $f = f_1$ and the period number p_2 in terms of single-frequency driving with $f = f_2$ differ in general, their period number must be equal in terms of dual-frequency driving with f_1 and f_2 to be able to drive the system smoothly (there is smooth dependence on the parameters) between Γ_1 and Γ_2 via the control surface introduced in Fig. 2e.

This section discusses how to select the frequency combinations to make the period numbers of the attrac-

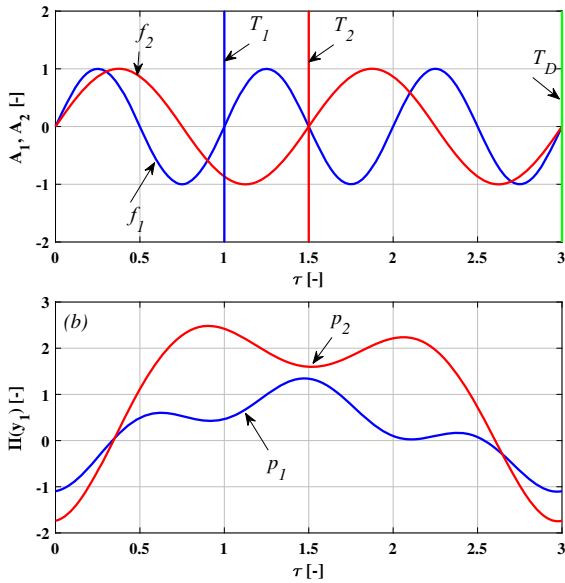


Fig. 3 An example to illustrate the period number and the torsion number compatibilities. **a** harmonic components of the dual-frequency driving signal. **b** two different periodic attractors in the single-frequency driven limit cases

tors along the curves Γ_1 and Γ_2 equal in terms of dual-frequency driving. Figure 3 demonstrates a hypothetical example. Panel (a) represents the components of the driving signal, while panel (b) shows the time series of periodic attractors of the corresponding single-frequency drivings. The colour coding is compatible with Fig. 2; namely, the blue and red curves are related to the orbits $\Gamma_1@f_1$ and $\Gamma_2@f_2$, respectively. The period of the f_1 component of the driving is T_1 , the period of the f_2 component of the driving is T_2 , and the period of the general dual-frequency driving is T_D . In Fig. 3, the time is normalised by T_1 ($\tau = t/T_1$).

Observe that the period number of the attractors along the curve Γ_1 is p_1 in terms of T_1 , but their period numbers are 1 in terms of T_D . Similarly, the period number of the attractors along the curve Γ_2 is p_2 in terms of T_2 ; however, their period numbers are again 1 in terms of T_D . Therefore, in the specific case plotted in Fig. 3, the period numbers of the orbits are equal if the Poincaré section is defined by T_D . The condition to achieve the period number equality/compatibility is

$$T_1 p_1 = T_2 p_2 = T_D, \tag{5}$$

which translates to

$$\frac{p_1}{p_2} = \frac{T_2}{T_1} = \frac{f_1}{f_2}. \tag{6}$$

The simple condition defined by Eq. (6) states that for a given pair of periodic orbits, the frequency ratio of the dual-frequency driving must be equal to the ratio of the period numbers. In general, any frequency combination with such a ratio is suitable. However, the curves Γ_1 and Γ_2 indicated by the thick vertical blue and red lines in Fig. 2a must exist in the parameter plane $A-f$ of the single-frequency driven case. This additional condition can limit the possible selection of the frequencies. For example, if f_1/f_2 is very small, then the value of f_2 can be larger than the upper bound of the red curves making it impossible to specify a second curve Γ_2 .

2.2 Torsion number compatibility

The second condition is related to the torsion number that describes the average number of rotations of a perturbed trajectory around a specific periodic orbit *during one period of the oscillation* [88]. In our second-order example systems, the torsion number is invariant (constant) near saddle-node (SN), period-doubling (PD) or symmetry-breaking (SB) bifurcation points [88] (i.e. along the green curves in Fig. 2e). In the systems studied here, only these three types of local bifurcations exist. Thus, the second condition reads as the pair-wise equality of the torsion numbers (q^a and q^b) of the bifurcation points $BF_1^a-BF_2^a$ and $BF_1^b-BF_2^b$. For a formal definition of the torsion number, the interested reader is referred to Appendix A. As the period of the oscillation of both orbits is equal to T_D (according to the period number compatibility), the second condition reads as

$$q_1^a = q_2^a = q^a, \tag{7}$$

$$q_1^b = q_2^b = q^b. \tag{8}$$

That is, the torsion numbers of the bounding bifurcation points of both the single and dual-frequency driving must be equal (pair-wise), see also Fig. 2.

2.3 Winding numbers: attractor selection possibilities in a Farey-tree

The period number and the torsion number compatibility can be discussed in terms of winding numbers. The winding number is in this context defined as the ratio of the torsion and the period number, $w = q/p$, and it characterises the organisation of resonances and bifurcation superstructures in the driving amplitude–frequency parameter plane (single frequency driving) [89–91]. These superstructures are usually organised according to a Farey-tree shown in Fig. 4. The interpretation is as follows: between two resonances/bifurcation curves having orders of $w_1 = q_1/p_1$ and $w_2 = q_2/p_2$, there is another one with an order of $w_3 = (q_1 + q_2)/(p_1 + p_2)$.

The Farey-tree can be an excellent tool to identify control possibilities between periodic orbits. First, if one intends to fulfil the torsion number equality condition, control is possible only between orbits having the same colour code in Fig. 4. Second, after selecting two orbits, the frequency ratio is adjusted according to the period numbers. Although there is no restriction for the period numbers, the relative sparsity of the elements with the same colour code in the Farey-tree is the main limitation of this approach; a detailed discussion is given in Sect. 5. It is to be stressed again that the winding numbers and the Farey-tree organisation are related to single-frequency driving. Dual-frequency driving is a temporary state of the control technique. Based on the knowledge presented in Fig. 4, the control process is demonstrated via several examples throughout Sects. 3 and 4 using the Toda and the Duffing oscillators.

Unfortunately, the period number and the torsion number compatibilities do not ensure the existence of a control surface, as demonstrated in Sects. 3 and 4. Therefore, they are necessary but not sufficient conditions.

3 Asymmetric case: Toda oscillator

The first test case is the Toda oscillator, which describes the output intensity of a solid-state laser in the transient regime [84]. The system of equations is adopted from [85] and reads as

$$\dot{y}_1 = y_2, \quad (9)$$

$$\dot{y}_2 = -dy_2 + e^{-y_1} - 1 + f_D(t), \quad (10)$$

where $d = 0.05$ is the damping constant and f_D denotes the general driving function, see Eqs. 3–4.

Before employing the control process, the first task is to explore the bifurcation structure of periodic orbits in the amplitude–frequency (A – f) parameter plane of the oscillator with the single frequency driving. It is a mandatory step for adequately selecting the orbits and frequency pairs for the control; see Sect. 2. Our strategy has the following steps: (a) generate orbit diagrams as a function of A with an initial-value problem (IVP) solver to perform a quick exploration of the periodic orbits, (b) compute the bifurcation curves of some selected periodic orbits (including the detection of bifurcation points) using a boundary value problem solver extended by pseudo-arc length parameter continuation (BVP-C), (c) determine the path of the detected bifurcation points in the A – f plane with the same BVP-C program package.

Figure 5a shows a one-dimensional orbit diagram with A as control parameter at a fixed frequency of $f = 2.5$. The black dots are the simulations with the IVP technique. Most of the branches of periodic orbits have a saddle-node (SN) bifurcation on the left and a period-doubling (PD) point on the right. Some of the winding numbers of the SN points are marked by bold fractions. Observe that their torsion numbers (numerators) are equal to unity; therefore, all of these orbits are suitable for our control process according to the torsion number compatibility given in Sect. 2.2. The proper choice of frequency combinations can easily fulfil the period number compatibility. Namely, any pair of these orbits can be selected, and the system can be driven from one orbit to another (and vice versa). Attractors corresponding to orders ($1/p$) are also computed via the BVP-C method (up to $p = 10$); in the figure, only the period-3 curves (blue) are shown for demonstration purposes. The green and the brown dots are the SN and PD points, respectively.

The paths of the detected SN (solid) and PD (dashed) bifurcation points are also computed in the A – f plane, see Fig. 5b. To avoid an overcrowded figure, only a few examples are plotted. Choosing the period-3 domain (enclosed by the curves $1/3$ and $1/6$) and the period-4 domain (enclosed by the curves $1/4$ and $1/8$), the frequency ratio must be $3/4$ according to Eq. 6. Thus, $f_1 = 3$ and $f_2 = 4$ are good candidates. During the control process, the amplitudes A_1 and A_2 of the driving are varied guiding the system between the two red vertical lines.

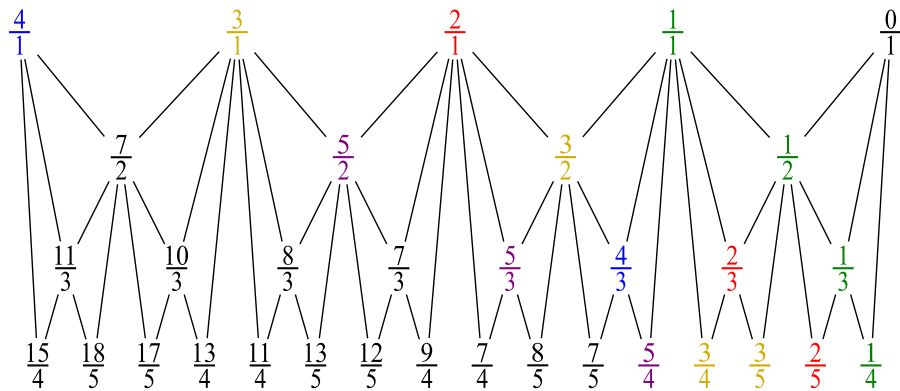


Fig. 4 Farey-tree as a tool to describe the organisation of periodic orbits in the driving frequency-amplitude parameter plane of a nonlinear oscillator. A fraction $w = q/p$ in the tree is the

winding number with torsion q and period number p . Between two elements $w_1 = q_1/p_1$ and $w_2 = q_2/p_2$, there is another one with a winding number of $w_3 = (q_1 + q_2)/(p_1 + p_2)$

For better visualisation of the period-3 and period-4 attractors, which are being transformed, their one-dimensional bifurcation curves are plotted in Fig. 6. The solid blue and the dashed red curves are stable and unstable solutions, respectively. Similarly, as in the case of Fig. 5b, the SN points are indicated by green dots, while the PD bifurcations are marked with brown dots. Although both panels of Fig. 6 are single frequency driven cases, the indices of the frequencies and the amplitudes are consistent with the forthcoming dual-frequency driving.

As a final step, the paths of the bifurcation points detected in Fig. 6 are computed as a function of the driving amplitudes A_1 and A_2 . The results are plotted in a three-dimensional diagram in Fig. 7a. The stable orbits shown in Fig. 6 of the single-frequency driving limit cases are also represented by the blue curves. Although only the bottom branches of the attractors are connected via the black curves, this proves the existence of a control surface that connects the period-3 and the period-4 attractors. Note that the surface itself is not calculated. Nevertheless, the system can be continuously driven from one attractor to another through this surface. The non-connecting curves are omitted in the diagram for clarity.

The test case presented in Fig. 7a is also demonstrated via an animation available as supplementary material. Three snapshots from the beginning, middle and end of the animation are shown in Fig. 8. Besides the three-dimensional representation, time series curves of the solutions and the driving signal

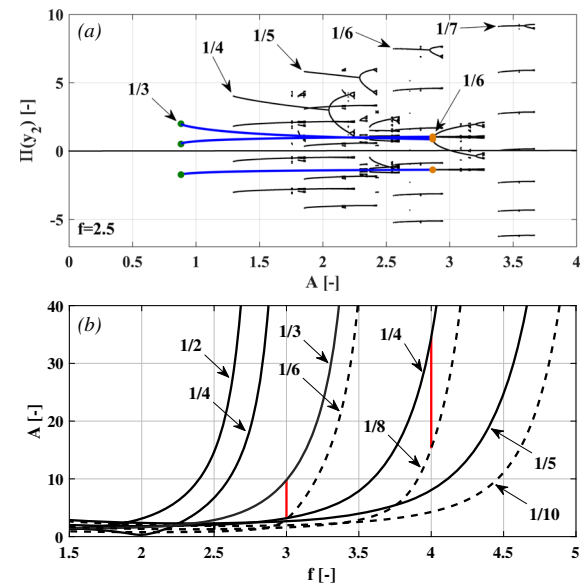


Fig. 5 Exploration of the periodic orbits of the Toda oscillator defined by Eqs. (9) and (10) with single frequency driving and a damping factor of $d = 0.05$. **a** one-dimensional orbit diagram where the second component of the Poincaré section is plotted as a function of the driving amplitude at a frequency of $f = 2.5$. **b** bifurcation curves in the $A-f$ plane of the detected bifurcation points (upper panel)

are also provided. The colour coding of the three-dimensional diagram is the same as in the case of Fig. 7a. The control process is initiated from a period-3 orbit and terminated at a period-4 orbit. The control parameters A_1 and A_2 are incremented after every 10 dual-frequency driving period along a straight line with

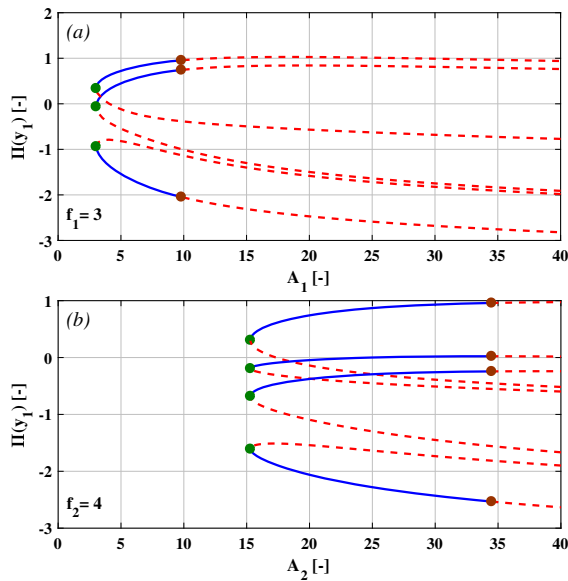


Fig. 6 Two examples of one-dimensional bifurcation diagrams computed by the BVP-C numerical method. The blue solid and dashed red curves are stable and unstable solutions, respectively. The green dots are SN points, while the brown dots are PD bifurcations. The control process presented in Fig. 7a is applied between these two types of attractors. **a** period-3 orbit. **b** period-4 orbit

a fine increment (the whole section is divided into 1000 points); see the thin red lines in the three-dimensional panels. The time series curves of x_1 are plotted in the top-right panels, where the blue curves represent solutions of the single-frequency driven limit cases, and the red curve is the solution of the temporary dual-frequency driving. In the bottom-right panels, the driving signals are plotted as a function of the dimensionless time: black curves are the single-frequency driving components, whereas the red curve is the temporary dual-frequency driving signal. Note that the red curve always coincides with one of the single-frequency-driven limit cases in the right-hand side panels for the first and last snapshots. For each snapshot, the control parameter values are also indicated.

Employing the same computational procedure, Fig. 7b shows another example between the period-5 and the period-3 orbits, where all the three branches of the period-3 curves are connected to other branches of the period-5 curves. Only the SN points are connected in the case of the two uppermost branches. Nevertheless, this already proves the existence of the corresponding control surfaces.

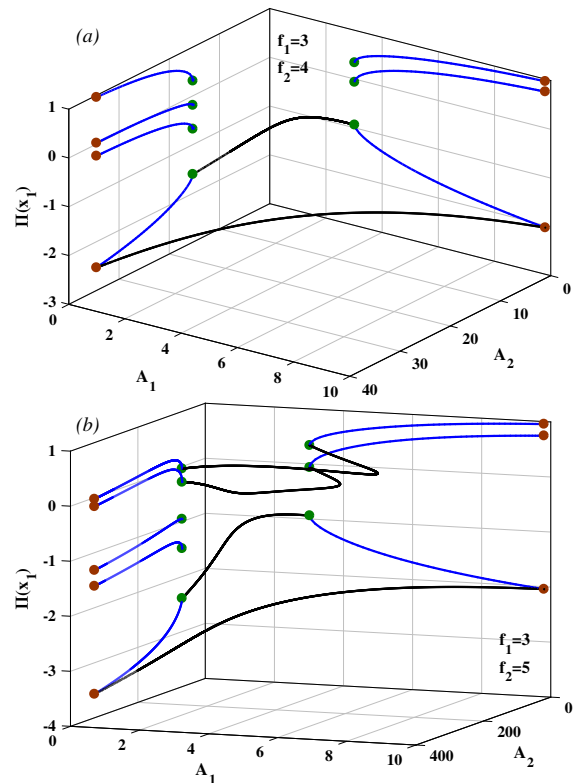


Fig. 7 Two examples of the existence of control surfaces between different periodic orbits of the Toda oscillator. **a** between a period-4 and a period-3 curves. **b** between a period-5 and a period-3 curves

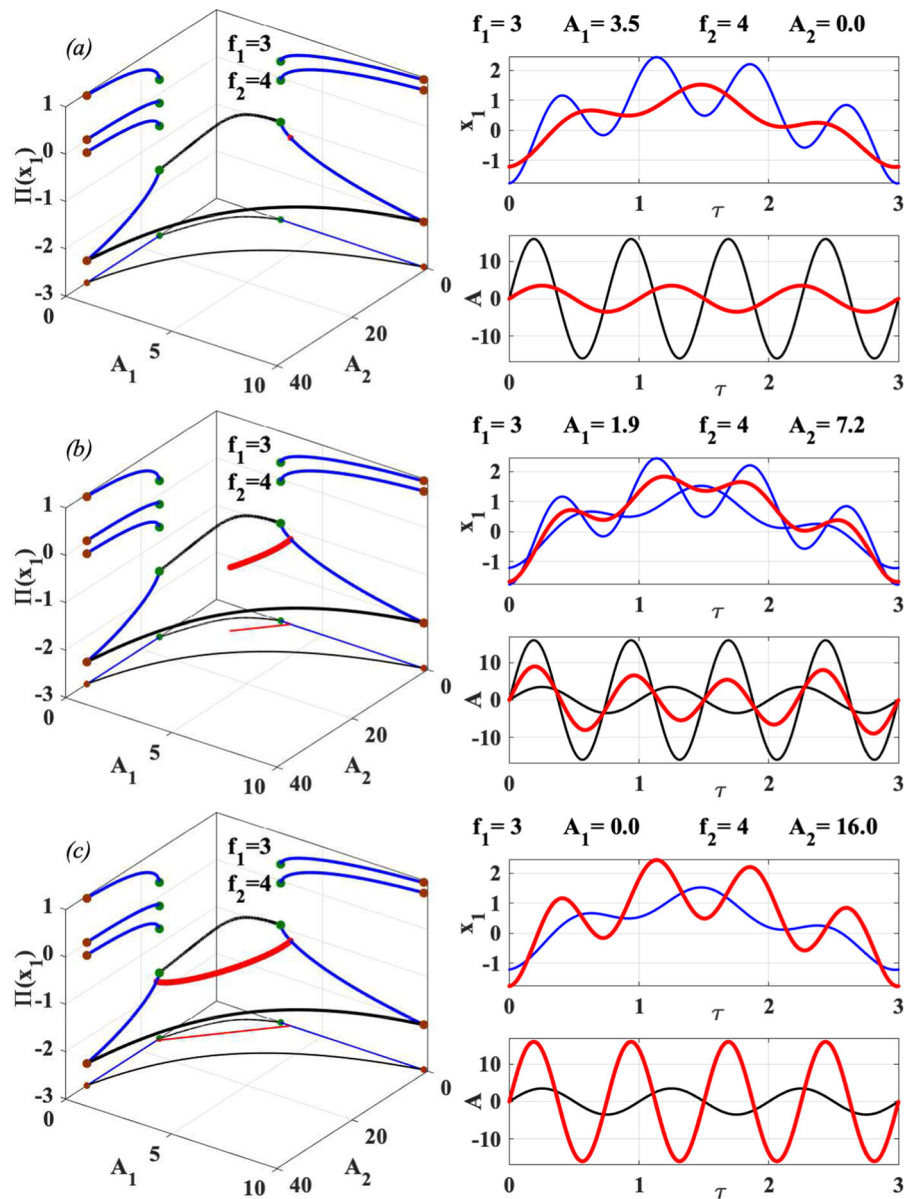
The existence of non-connected branches of the bifurcation diagrams of the periodic attractors has important consequences. Initiating the attractor targeting process from a period-3 orbit, the period-5 attractor can safely be reached according to Fig. 7b (all branches are connected). However, driving the system, e.g. from the period-4 or period-5 orbits to the period-3 attractor, the control process can be successful only with the correct initial phase. A detailed “safe routes” discussion between attractors is discussed in [83].

Although it is not shown in this section, a transformation between any periodic orbits marked by the bold fractions in Fig. 5a is possible. Therefore, it is demonstrated that our attractor targeting technique also works for the asymmetric Toda oscillator. The following section deals with the symmetric Duffing system.

4 Symmetric case: Duffing oscillator

The second test case is the symmetric Duffing oscillator [86], which models, for instance, an elastic pendulum

Fig. 8 Three snapshots from the animation (provided as a supplementary material) of the control process presented in Fig. 7a. **a** beginning of the control process, single-frequency driving ($A_2 = 0$). **b** middle of the control process, dual-frequency driving. **c** end of the control process, single-frequency driving ($A_1 = 0$). In the right column, the corresponding oscillations of the first variable x_1 and the driving signals A are given as functions of the dimensionless time τ . For the colour codes, see the corresponding discussion of the main text



with non-Hookean spring stiffness. The double-well version is written as

$$\dot{y}_1 = y_2, \tag{11}$$

$$\dot{y}_2 = y_1 - y_1^3 - d y_2 + f_D(t), \tag{12}$$

where d is the damping constant and f_D denotes the general driving function, see Eqs. 3–4 again. In the case of the Toda system, the control surfaces were easy to visualise with their bounding bifurcation curves. In contrast, the visualisation of the control surfaces of the Duffing oscillator can be a real challenge due to their complexity. Nevertheless, it is still sufficient to com-

pute some bounding curves to prove their existence. Since the system is smooth in terms of state space and parameters, there is a continuous dependence on the initial conditions and parameters. Therefore, at least small stripes exist near the bounding bifurcation curves, which represent the control surface. With increasing damping factor d , the complexity of the control surfaces is reduced. However, a high damping rate might not be achievable in applications, and the number of available attractors is also reduced (low opportunity of suitable attractor selection). Therefore, in the next

two subsections, cases with a high and a low damping rate are discussed to demonstrate its effect on the complexity of the surface. The technical procedure of computations is already discussed in Sect. 3 in detail; thus, it is omitted here, and only the control surfaces are depicted in three-dimensional diagrams similar to Fig. 7.

4.1 High damping

Figure 9 shows an example of a control surface between period-1 and period-3 orbits at a damping rate of $d = 0.3$. With $A_2 = 0$, the period-1 curve is bounded by a saddle-node (SN, green dot) and a symmetry breaking (SB, black dot) bifurcation with winding numbers $1/1$ and $2/1$, respectively. For the single-frequency driven limit case of $A_1 = 0$, two segments of period-3 curves exist (one around $A_2 = 3$ and another near $A_2 = 10$). They are also bounded by a SN and a SB bifurcation. The corresponding winding numbers are $1/3$ and $2/3$. Since the torsion numbers of all SN points match, connections between the green points are to be expected. For the same reasons, it is true for all the black SB points. To place the control problem in the Farey-tree, see the corresponding green and red fractions in Fig. 4. To satisfy the period number condition introduced in Sect. 2.1, the frequency combination is set to $f_1 = 1$ and $f_2 = 3$. Observe that this example is in the domain of harmonic resonances (orders $w = q/p$, where $q > 1$), while all the cases of the Toda oscillator were related to subharmonic resonances (orders $w = 1/p$).

In Fig. 9, only the dual-frequency bifurcation curves that connect two dots are presented (black curves). There is only a single control surface; however, it connects three branches of the period-3 orbits and the single period-1 curve. Such a surface is multivalued over the A_1 – A_2 parameter plane indicating co-existence of attractors. Their origin is a cusp bifurcation shown in the projection of the curve connecting the two green dots of orders $1/3$ (solid thin line in the A_1 – A_2 plane). A special feature of this control surface is that it enables the transition between the two disjoint period-3 segments that are present at the same driving frequency ($f_2 = 3$). There is no direct connection between these period-3 segments, e.g. by forward-reversed period doubling sequences without changing f_2 . Therefore, the temporary dual-frequency driving is also suitable

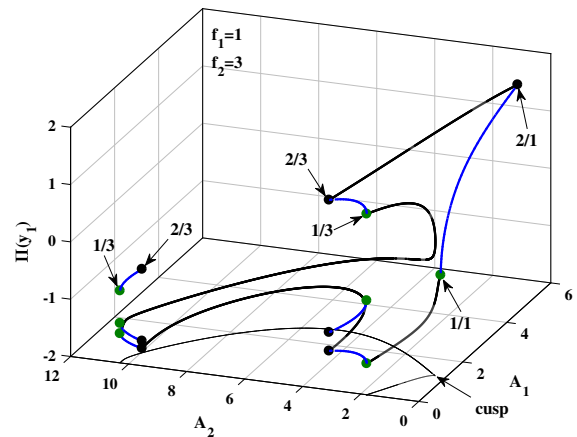


Fig. 9 Examples of the existence of a control surface between period-1 and period-3 orbits of the Duffing oscillator with high damping ($d = 0.3$)

for guiding the system between attractors with the same period numbers and driven with the same frequency value.

4.2 Low damping

In general, decreasing the damping rate of a system leads to a higher number of attractors in a given parameter domain. For a damping rate of $d = 0.02$, the situation of densely “packed” periodic attractors is already demonstrated in Fig. 1 for the single-frequency driven Duffing oscillator. This also leads to more options for attractor selection. However, the shape of the control surfaces can be extremely complex, causing difficulties not only in visualisation but also from an application point of view as the control process occurs along an intricate surface that needs to be known in advance.

An example is shown in Fig. 10 for $d = 0.02$. The colour coding of the (bifurcation) curves and the bifurcation points is the same as in the case of the high damping example depicted in Fig. 9. At the single-frequency driven limit case of $A_2 = 0$, two segments of period-1 orbits exist; see the blue curves and the corresponding winding numbers of $4/1$ and $5/1$. When $A_1 = 0$, two disjoint period-3 curves exist bounded by SN and SB points having winding numbers of $4/3$ and $5/3$. Again, the main goal is to locate bifurcation curves in the dual-frequency driven A_1 – A_2 parameter plane, which connects two SN or two SB points. Altogether, three such curves are identified and shown in Fig. 10. One black curve connects SB points of orders $5/3$ and $4/3$, and the other one connects the points of orders $4/1$

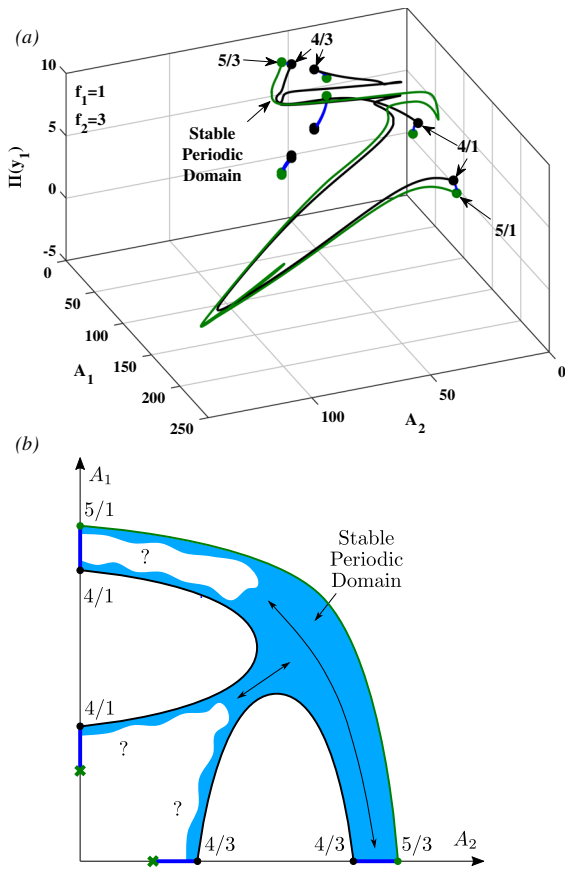


Fig. 10 Examples of the existence of a control surface between period-1 and period-3 orbits of the Duffing system with low damping ($d = 0.02$). **a** a three-dimensional representation of the bifurcation curves and the control surface. **b** a simplified sketch of the bifurcation structure projected to the A_1 – A_2 plane and $5/1$. Note that their initial and final states are at the same single-frequency driven limit case; therefore, they cannot ensure the existence of a control surface. On the other hand, the green bifurcation curve connects a period-3 curve (SN point of order $5/3$) and a period-1 curve (SN point of order $5/1$). That is, the existence of a control surface is proven.

As the black and green curves depicted in Fig. 10 are folded several times, the shape of the control surface is hard to visualise. Therefore, a simplified sketch of their projection into the A_1 – A_2 plane is provided in Fig. 10b. Although the two black curves are separated, they move close to each other in a specific region of the parameter plane. We verified that the black curves are connected with periodic attractors near their shortest distance with additional simulations. Similarly, it is also verified that this domain of stable periodic attractors extends towards the period-3 single-frequency bifur-

cation curve bounded by points $4/3$ and $4/3$. The light blue shaded domain shows this validated piece of the control surface in the pictogram. Since the Duffing oscillator is smooth, it is also evident that the control surface exists close to the black and green bifurcation curves. Thus, with proper tuning of the amplitudes, one can guide the system between any of the four branches of the single-frequency driven bifurcation segments (thick, blue lines along the A_1 and A_2 axes).

Far from the light blue region, the shape of the control surface is (still) unidentified; see the question marks in Fig. 10b. The unconnected SN points marked by the green crosses in the pictogram are connected to other single-frequency driven bifurcation branches of periodic orbits (not shown here for clarity). This indicates that the control surface has several branches and overlapping layers connecting several disjunct curves of periodic orbits in the single-frequency driven limit cases. The complexity of the black and green curves shown in Fig. 10a implies that even when computing all bounding curves of the control surface, its exact shape could still be hard to visualise and identify. Thus, the complete mapping of the control surface is beyond the scope of the present paper; the primary objective of proving its existence has already been achieved.

5 Discussion

The main advantage of the presented control method is the possibility of attractor selection without applying feedback to the system. Therefore, it can be a viable option for applications where feedback is impossible to achieve. Thus, it is a gap-filling technique compared to the existing method available in the literature [59]. It is shown that this control method works for different nonlinear oscillators and between different periodic attractors. The Farey-tree helps to identify possible periodic orbits for attractor selection corresponding to the period and torsion number compatibility.

However, attractor selection possibility without feedback also poses problems for the user. First, the control surface through which the control process is realised must be known in advance. In addition, this surface can be highly complex, which makes it difficult to apply this control in practice. A remedy to this issue can be to still apply some form of feedback. However, as the primary goal here is to approximate the position of the

system in the control surface, precise information about the state of the system or its Jacobian would still be not necessary. For example, if the Duffing oscillator is a model equation of an elastic pendulum, the harmonic, subharmonic and ultraharmonic peaks in the Fourier-transform of the force on the spring could be a tool to identify the system on a control surface. The reason for this possibility is that winding numbers (which are the key components in the Farey-tree) usually appear in the spectrum of such an indirect quantity. As an example, see the spectral bifurcation diagram of the emitted pressure of a harmonically driven bubble in [92].

Another limitation arises when the control of multistability is the objective. Applications might require fixed or only slightly modified operating parameters. However, significant variations (albeit temporary) in the control parameters are necessary during our control process. Thus, this technique is suitable only for systems where such a temporary large deviation is feasible.

The period number compatibility is relatively easy to satisfy: it needs the application of proper frequency combinations. Using the Farey-tree to identify possible attractor targeting possibilities, however, the most significant constraint is the torsion number compatibility condition; see the relatively sparse options highlighted in Fig. 4. The torsion number compatibility is a necessary condition if one seeks bifurcation curves that establish a direct connection between the selected two kinds of periodic orbits, see the configuration illustrated in Fig. 2c. Nevertheless, the results shown in Fig. 10 imply that although the black curves make no connections between the corresponding single-frequency driven attractors, control is still possible due to the existing stable domain between them (light blue domain). Thus, fulfilling the torsion number compatibility is advantageous but is not a necessary condition when control routes exist that do not follow a bifurcation curve.

The last issue is related to the computational and visualisation difficulties of possibly complex control surfaces (e.g. the low damping case of the Duffing oscillator). In our previous papers [77, 83], we employed the “brute-force” approach; that is, the parameter plane A_1 – A_2 is scanned with a fine resolution by applying several randomised initial conditions (to reveal coexisting attractors). It worked fine with a relatively simple control surface such as the bubble oscillator [83] or the Toda system (discussed in the present study). How-

ever, for the extremely rich bifurcation structure of the Duffing equation, e.g. Fig. 1, the number of the initial conditions at a given parameter combination had to be as high as 400 to obtain sufficiently smooth surfaces. The required high resolution of the parameters and the large number of initial conditions leads to difficulties in visualisation: the real-time inspection (rotation, magnification) of the tens or hundreds of millions of data points is a cumbersome task causing difficulties in the post-processing phase. Therefore, the approach of the present study was to directly compute the bounding bifurcation curves of the control surfaces with the BVP-C approach, which is fast and does not need the treatment of millions of data points. However, as the results in Sect. 4.2 demonstrated, it cannot solve the visualisation difficulties if the control surface has a very complicated shape. To resolve the above-described visualisation issues, the application of an automated surface reconstruction algorithm together with a proper parameter continuation is mandatory.

6 Summary

The present study introduces a novel attractor selection technique applicable to harmonically driven nonlinear oscillators. It is based on the observation that two periodic attractors that cannot be transformed into each other by tuning the system parameters may be transformed continuously by temporarily adding a second harmonic component to the driving. A necessary but not sufficient condition is the equality of the ratio of the period numbers of the two attractors and the ratio of the frequency component of the temporary dual-frequency driving. Another necessary but not sufficient condition is the equality of the torsion numbers of the bounding bifurcation points of the domain of periodic orbits being transformed. The method was successfully tested on the Toda and the Duffing nonlinear oscillators.

Funding Open Access funding enabled and organized by Projekt DEAL. The research reported in this paper is part of project no. BME-NVA-02, implemented with the support provided by the Ministry of Innovation and Technology of Hungary from the National Research, Development and Innovation Fund, financed under the TKP2021 funding scheme. This paper was supported by the János Bolyai Research Scholarship of the Hungarian Academy of Sciences, by the New National Excellence Program of the Ministry of Human Capacities (Ferenc Hegedűs: ÚNKP-21-5-BME-369) and by the NVIDIA Corporation via the Academic Hardware Grants Program. The authors acknowledge the

financial support of the Hungarian National Research, Development and Innovation Office via NKFIH grant OTKA FK142376.

Data availability The datasets generated during and/or analysed during the current study are available from the corresponding author on reasonable request.

Declarations

Competing interests The authors have not disclosed any competing interests.

Open Access This article is licensed under a Creative Commons Attribution 4.0 International License, which permits use, sharing, adaptation, distribution and reproduction in any medium or format, as long as you give appropriate credit to the original author(s) and the source, provide a link to the Creative Commons licence, and indicate if changes were made. The images or other third party material in this article are included in the article’s Creative Commons licence, unless indicated otherwise in a credit line to the material. If material is not included in the article’s Creative Commons licence and your intended use is not permitted by statutory regulation or exceeds the permitted use, you will need to obtain permission directly from the copyright holder. To view a copy of this licence, visit <http://creativecommons.org/licenses/by/4.0/>.

Appendix A: Torsion number calculation

In what follows, we want to give a general expression for the computation of the torsion number according to [88]. The systems studied here may be subdivided as:

$$\ddot{x} + g(x, \dot{x}) = h(t) \tag{13}$$

where $h(t)$ is a $T = 2\pi/\omega$ periodic driving, i.e. $h(t + T) = h(t)$. For example, in the case of the Duffing oscillator, $g(x, \dot{x}) = \delta\dot{x} + \beta x + \alpha x^3$ and $h(t) = A \cos(\omega t)$, equation (13) may be reduced to a first-order system of differential equations:

$$\begin{aligned} \dot{x}_1 &= x_2, \\ \dot{x}_2 &= -g(x_1, x_2) + h(Tx_3), \\ \dot{x}_3 &= \frac{1}{T} = \frac{\omega}{2\pi}. \end{aligned} \tag{14}$$

The Poincaré map of this system is obtained by the stroboscopic map

$$(x_1(t), x_2(t)) \mapsto (x_1(t + T), x_2(t + T)). \tag{15}$$

To compute the torsion number, we consider the time evolution of an infinitesimally small perturbation, y , of a fixed point of the corresponding Poincaré map, corresponding to some periodic orbit which is given by [88]:

$$\ddot{y} + \frac{\partial g}{\partial x_2}(x_1, x_2)\dot{y} + \frac{\partial g}{\partial x_1}(x_1, x_2)y = 0, \tag{16}$$

and thus,

$$\dot{y}_1 = y_2, \tag{17}$$

$$\dot{y}_2 = -\frac{\partial g}{\partial x_1}y_1 - \frac{\partial g}{\partial x_2}y_2. \tag{18}$$

The solutions of this variational equation system, $\mathbf{u}(t) = (u_1(t), u_2(t))$, describe spiral-like curves in the tangent space $\{(y, \dot{y})\}$ from which the number of torsions of the perturbed orbit around the periodic reference orbit is calculated. Rewriting \mathbf{u} in polar coordinates, (r, ϑ) , the angular velocity reads:

$$\dot{\vartheta}(t) = \frac{d}{dt} \frac{\sin \vartheta}{\cos \vartheta} = \frac{u_1\dot{u}_2 - \dot{u}_1u_2}{u_1^2 + u_2^2}. \tag{19}$$

The average torsion frequency is given by

$$\Omega(\gamma) := \lim_{t \rightarrow \infty} \frac{1}{t} \left| \int_0^t \dot{\vartheta}(t') dt' \right|. \tag{20}$$

Thus, the torsion number q of a period- m orbit is finally defined by [88]:

$$\begin{aligned} q &= m \frac{\Omega}{T/2\pi} \\ &= \frac{m}{\omega} \lim_{t \rightarrow \infty} \frac{1}{t} \left| \int_0^t \frac{u_1\dot{u}_2 - \dot{u}_1u_2}{u_1^2 + u_2^2} dt' \right|, \quad m \in \mathbb{N}, \end{aligned} \tag{21}$$

where m is the period number of the orbit, i.e. $x_j(t) = x_j(t + mT)$.

References

1. Lorenz, E.N.: Deterministic nonperiodic flow. *J. Atmos. Sci.* **20**(2), 130 (1963)

2. Rajagopal, K., Pham, V.T., Alsaadi, F.E., Alsaadi, F.E., Karthikeyan, A., Duraisamy, P.: Multistability and coexisting attractors in a fractional order Coronary artery system. *Eur. Phys. J. Spec. Top.* **227**, 837 (2018)
3. Pati, N.C., Layek, G.C., Pal, N.: Bifurcations and organized structures in a predator-prey model with hunting cooperation. *Chaos, Solitons and Fractals* **140**, 110184 (2020)
4. Hossain, M., Pal, S., Tiwari, P.K., Pal, N.: Bifurcations, chaos, and multistability in a nonautonomous predator-prey model with fear. *Chaos* **31**(12), 123134 (2021)
5. Pati, N.C., Garai, S., Hossain, M., Layek, G.C., Pal, N.: Fear Induced Multistability in a Predator-Prey Model. *Int. J. Bifurc. Chaos* **31**(10), 2150150 (2021)
6. Debbouche, N., Ouannas, A., Momani, S., Cafagna, D., Pham, V.T.: Fractional-order biological system: chaos, multistability and coexisting attractors. *Eur. Phys. J. Spec. Top.* **231**, 1061 (2022)
7. Freire, J.G., Calderón-C, A., Varela, H., Gallas, J.A.C.: Phase diagrams and dynamical evolution of the triple-pathway electro-oxidation of formic acid on platinum. *Phys. Chem. Chem. Phys.* **22**(3), 1078 (2020)
8. Field, R.J., Freire, J.G., Gallas, J.A.C.: Quint points lattice in a driven Belousov–Zhabotinsky reaction model. *Chaos* **31**(5), 053124 (2021)
9. Olsen, L.F., Lunding, A.: Chaos in the peroxidase-oxidase oscillator. *Chaos* **31**(1), 013119 (2021)
10. Adéchinan, A.J., Kpomahou, Y.J.F., Hinvi, L.A., Miwadinou, C.H.: Chaos, coexisting attractors and chaos control in a nonlinear dissipative chemical oscillator. *Chin. J. Phys.* **77**, 2684 (2022)
11. Short, K.Y.: Periodic solutions and chaos in the Barkley pipe model on a finite domain. *Phys. Rev. E* **100**(2), 023116 (2019)
12. Garcia, F., Seilmayer, M., Giesecke, A., Stefani, F.: Chaotic wave dynamics in weakly magnetized spherical Couette flows. *Chaos* **30**(4), 043116 (2020)
13. Kanchana, C., Su, Y., Zhao, Y.: Regular and chaotic Rayleigh–Bénard convective motions in methanol and water. *Commun. Nonlinear Sci. Numer. Simul.* **83**, 105129 (2020)
14. Pati, N.C., Rech, P.C., Layek, G.C.: Multistability for nonlinear acoustic-gravity waves in a rotating atmosphere. *Chaos* **31**(2), 023108 (2021)
15. Alexandrov, D.V., Bashkirtseva, I.A., Crucifix, M., Ryashko, L.B.: Nonlinear climate dynamics: from deterministic behaviour to stochastic excitability and chaos. *Phys. Rep.* **902**, 1 (2021)
16. Jánosi, D., Károlyi, G., Tél, T.: Climate change in mechanical systems: the snapshot view of parallel dynamical evolutions. *Nonlinear Dyn.* **106**, 2781 (2021)
17. Rocha, R., Medrano-T, R.O.: Stability analysis for the Chua circuit with cubic polynomial nonlinearity based on root locus technique and describing function method. *Nonlinear Dyn.* **102**, 2859 (2020)
18. Rocha, R., Medrano-T, R.O.: Chua circuit based on the exponential characteristics of semiconductor devices. *Chaos, Solitons and Fractals* **156**, 111761 (2022)
19. Pradhan, B., Saha, A., Natiq, H.: Multistability and dynamical properties of quantum ion-acoustic flow. *Eur. Phys. J. Spec. Top.* **230**, 1503 (2021)
20. Chandra, S., Kapoor, S., Nandi, D., Das, C., Bhattacharjee, D.: Bifurcation analysis of EAWs in degenerate astrophysical plasma: chaos and multistability. *IEEE Trans. Plasma Sci.* **50**(6), 1495 (2022)
21. Li, N., Susanto, H., Cemlyn, B.R., Henning, I.D., Adams, M.J.: Mapping bifurcation structure and parameter dependence in quantum dot spin-VCSELs. *Opt. Exp.* **26**(11), 14636 (2018)
22. Pisarchik, A.N., Hramov, A.E.: *Multistability in Lasers*, pp. 167–198. Springer International Publishing, Cham (2022)
23. Meucci, R., Marc Ginoux, J., Mehrabbeik, M., Jafari, S., Clinton Sprott, J.: Generalized multistability and its control in a laser. *Chaos* **32**(8), 083111 (2022)
24. Mas Arabí, C., Englebort, N., Parra-Rivas, P., Gorza, S.P., Leo, F.: Mode-locking induced by coherent driving in fiber lasers. *Opt. Lett.* **47**(14), 3527 (2022)
25. Kadar, F., Hös, C., Stepan, G.: Delayed oscillator model of pressure relief valves with outlet piping. *J. Sound Vib.* **534**, 117016 (2022)
26. Bartfai, A., Dombovari, Z.: Hopf bifurcation calculation in neutral delay differential equations: Nonlinear robotic arms subject to delayed acceleration feedback control. *Int. J. Non-Linear Mech.* **147**, 104239 (2022)
27. Lu, H., Stepan, G., Lu, J., Takacs, D.: Dynamics of vehicle stability control subjected to feedback delay. *Eur. J. Mech. A Solids* **96**, 104678 (2022)
28. Habib, G., Bártfai, A., Barrios, A., Dombovári, Z.: Bistability and delayed acceleration feedback control analytical study of collocated and non-collocated cases. *Nonlinear Dyn.* **108**, 2075 (2022)
29. Danca, M.F., Fečkan, M.: Hidden chaotic attractors and chaos suppression in an impulsive discrete economical supply and demand dynamical system. *Commun. Nonlinear Sci. Numer. Simul.* **74**, 1 (2019)
30. Yousefpour, A., Jahanshahi, H., Munoz-Pacheco, J.M., Bekiros, S., Wei, Z.: A fractional-order hyper-chaotic economic system with transient chaos. *Chaos, Solitons and Fractals* **130**, 109400 (2020)
31. Barnett, W.A., Bella, G., Ghosh, T., Mattana, P., Venturi, B.: Shilnikov chaos, low interest rates, and New Keynesian macroeconomics. *J. Econ. Dyn. Control* **134**, 104291 (2022)
32. Galatzer-Levy, R., Moran, G., Rose, J., Shulman, G., Whittle, P.: *The Non-linear Mind: Psychoanalysis of Complexity in Psychic Life*, 1st edn. Routledge, Milton Park (2016)
33. Feigenbaum, M.J.: Quantitative universality for a class of nonlinear transformations. *J. Stat. Phys.* **19**(1), 25 (1978)
34. Nuño, J.C., Muñoz, F.J.: The partial visibility curve of the Feigenbaum cascade to chaos. *Chaos, Solitons and Fractals* **131**, 109537 (2020)
35. Layek, G.C., Pati, N.C.: Period-bubbling transition to chaos in thermo-viscoelastic fluid systems. *Int. J. Bifurc. Chaos* **30**(06), 2030013 (2020)
36. Nuño, J.C., Muñoz, F.J.: Universal visibility patterns of unimodal maps. *Chaos* **30**(6), 063105 (2020)
37. Parlitz, U., Lauterborn, W.: Period-doubling cascades and devil's staircases of the driven van der Pol oscillator. *Phys. Rev. A* **36**(3), 1428 (1987)
38. Englisch, V., Lauterborn, W.: The winding-number limit of period-doubling cascades derived as Farey-fraction. *Int. J. Bifurc. Chaos* **4**(4), 999 (1994)
39. Goldberg, L., Tresser, C.: Rotation orbits and the Farey tree. *Ergod. Theory Dyn. Syst.* **16**(5), 1011 (1996)

40. Hegedűs, F.: Topological analysis of the periodic structures in a harmonically driven bubble oscillator near Blake's critical threshold: Infinite sequence of two-sided Farey ordering trees. *Phys. Lett. A* **380**(9–10), 1012 (2016)
41. Goldin, A.Y., Kasimov, A.R.: Synchronization of detonations: Arnold tongues and devil's staircases. *J. Fluid Mech.* **946**, R1 (2022)
42. Wu, X., Zhang, Y., Peng, J., Boscolo, S., Finot, C., Zeng, H.: Farey tree and devil's staircase of frequency-locked breathers in ultrafast lasers. *Nat. Commun.* **13**, 5784 (2022)
43. Medeiros, E.S., Medrano-T, R.O., Caldas, I.L., de Souza, S.L.T.: Torsion-adding and asymptotic winding number for periodic window sequences. *Phys. Lett. A* **377**(8), 628 (2013)
44. Layek, G.C., Pati, N.C.: Organized structures of two bidirectionally coupled logistic maps. *Chaos* **29**(9), 093104 (2019)
45. Nicolau, N.S., Oliveira, T.M., Hoff, A., Albuquerque, H.A., Manchein, C.: Tracking multistability in the parameter space of a Chua's circuit model. *Eur. Phys. J. B* **92**, 106 (2019)
46. Varga, R., Klapcsik, K., Hegedűs, F.: Route to shrimps: dissipation driven formation of shrimp-shaped domains. *Chaos, Solitons and Fractals* **130**, 109424 (2020)
47. Santana, L., da Silva, R.M., Albuquerque, H.A., Manchein, C.: Transient dynamics and multistability in two electrically interacting FitzHugh–Nagumo neurons. *Chaos* **31**(5), 053107 (2021)
48. Manchein, C., Santana, L., da Silva, R.M., Beims, M.W.: Noise-induced stabilization of the FitzHugh–Nagumo neuron dynamics: multistability and transient chaos. *Chaos* **32**(8), 083102 (2022)
49. Trobia, J., de Souza, S.L.T., dos Santos, M.A., Szezech, J.D., Batista, A.M., Borges, R.R., Pereira, Ld.S., Protachevich, P.R., Caldas, I.L., Iarosz, K.C.: On the dynamical behaviour of a glucose-insulin model. *Chaos, Solitons and Fractals* **155**, 111753 (2022)
50. Bonatto, C., Gallas, J.A.C., Ueda, Y.: Chaotic phase similarities and recurrences in a damped-driven Duffing oscillator. *Phys. Rev. E* **77**(2), 026217 (2008)
51. Medeiros, E.S., de Souza, S.L.T., Medrano-T, R.O., Caldas, I.L.: Replicate periodic windows in the parameter space of driven oscillators. *Chaos Solitons Fractals* **44**(11), 982 (2011)
52. Shi, J.F., Zhang, Y.L., Gou, X.F.: Bifurcation and evolution of a forced and damped Duffing system in two-parameter plane. *Nonlinear Dyn.* **93**, 749 (2018)
53. Zhang, X.F., Zheng, J.K., Wu, G.Q., Bi, Q.S.: Mixed mode oscillations as well as the bifurcation mechanism in a Duffing's oscillator with two external periodic excitations. *Sci. China Technol. Sci.* **62**, 1816 (2019)
54. Stankevich, N.V., Dvorak, A., Astakhov, V., Jaros, P., Kapitaniak, M., Perlikowski, P., Kapitaniak, T.: Chaos and Hyperchaos in Coupled Antiphase Driven Toda Oscillators. *Regul. Chaotic Dyn.* **23**(1), 120 (2018)
55. Kolebaje, O., Popoola, O.O., Vincent, U.E.: Occurrence of Vibrational resonance in an oscillator with an asymmetric Toda potential. *Phys. D* **419**, 132853 (2021)
56. El-Dib, Y.O., Mady, A.A.: The non-conservative forced Toda oscillator. *J. Appl. Math. Mech.* **102**(4), e202100379 (2022)
57. da Silva, A., Pati, N.C., Rech, P.C.: Multistability and period-adding in a logarithmic Lorenz system. *Int. J. Mod. Phys. C* **33**(5), 2250062 (2022)
58. Rech, P.C.: Periodicity suppression and period-adding caused by a parametric excitation in the Lorenz system. *Eur. Phys. J. B* **95**, 169 (2022)
59. Pisarchik, A.N., Feudel, U.: Control of multistability. *Phys. Rep.* **540**(4), 167 (2014)
60. Chizhevsky, V.N., Grigorieva, E.V., Kashchenko, S.A.: Optimal timing for targeting periodic orbits in a loss-driven CO₂ laser. *Opt. Commun.* **133**(1), 189 (1997)
61. Andreev, A.V., Frolov, N.S., Alexandrova, N.A., Chaban, M.A.: In Saratov Fall Meeting 2019: Computations and Data Analysis: from Nanoscale Tools to Brain Functions, ed. by Postnov, D.E.: International Society for Optics and Photonics, SPIE, vol. 11459, p. 114590W (2020)
62. di Marco, M., Forti, M., Moretti, R., Pancioni, L., Innocenti, G., Tesi, A.: Feedforward control of multistability in memristor circuits. In: 2021 28th IEEE International Conference on Electronics, Circuits, and Systems (ICECS), pp. 1–6 (2021)
63. Parker, J., Bondy, B., Prilutsky, B.I., Cymbalyuk, G.: Control of transitions between locomotor-like and paw shake-like rhythms in a model of a multistable central pattern generator. *J. Neurophysiol.* **120**(3), 1074 (2018)
64. Pisarchik, A.N., Goswami, B.K.: Annihilation of one of the coexisting attractors in a bistable system. *Phys. Rev. Lett.* **84**(7), 1423 (2000)
65. Yang, J., Jing, Z.: Control of chaos in a three-well duffing system. *Chaos Solitons Fractals* **41**(3), 1311 (2009)
66. Chacón, R., García-Hoz, A.M., Miralles, J.J., Martínez, P.J.: Amplitude modulation control of escape from a potential well. *Phys. Lett. A* **378**(16), 1104 (2014)
67. Zhou, Z.X., Ren, H.P., Grebogi, C.: Suppressing chaos in crystal growth process using adaptive phase resonant perturbation. *Nonlinear Dyn.* **108**, 2655 (2022)
68. Shinbrot, T., Ott, E., Grebogi, C., Yorke, J.A.: Using chaos to direct trajectories to targets. *Phys. Rev. Lett.* **65**, 3215 (1990)
69. Jiang, Y.: Trajectory selection in multistable systems using periodic drivings. *Phys. Lett. A* **264**(1), 22 (1999)
70. Sami Doubla, I., Ramakrishnan, B., Tabekoueng Njitacke, Z., Kengne, J., Rajagopal, K.: Hidden extreme multistability and its control with selection of a desired attractor in a non-autonomous Hopfield neuron. *AEU Int. J. Electron. Commun.* **144**, 154059 (2022)
71. Zhang, Z., Páez Chávez, J., Sieber, J., Liu, Y.: Controlling grazing-induced multistability in a piecewise-smooth impacting system via the time-delayed feedback control. *Nonlinear Dyn.* **107**, 1595 (2022)
72. Geisler, R., Kurz, T., Lauterborn, W.: Acoustic bubble traps. In: AIP Conference Proceedings vol. 524(1), p. 417 (2000)
73. Zhou, Z.X., Ren, H.P., Grebogi, C.: Bi-directional impulse chaos control in crystal growth. *Chaos* **31**(5), 053106 (2021)
74. Kaneko, K.: Dominance of milnor attractors and noise-induced selection in a multiattractor system. *Phys. Rev. Lett.* **78**, 2736 (1997)
75. Zerega, B., Pisarchik, A.N.: In: Sixth Symposium Optics in Industry, vol. 6422, ed. by J.C. Gutiérrez-Vega, J. Dávila-Rodríguez, C. López-Mariscal. International Society for Optics and Photonics, vol. 6422, p. 64221J. SPIE (2007)

76. Shajan, E., Shrimali, M.D.: Controlling multistability with intermittent noise. *Chaos Solitons Fract.* **160**, 112187 (2022)
77. Hegedűs, F., Lauterborn, W., Parlitz, U., Mettin, R.: Non-feedback technique to directly control multistability in nonlinear oscillators by dual-frequency driving. *Nonlinear Dyn.* **94**(1), 273 (2018)
78. Lauterborn, W., Ohl, C.D.: *Acoustic Cavitation and Multi-Bubble Sonoluminescence*, pp. 97–104. Springer, Dordrecht (1999)
79. Storey, B.D., Szeri, A.J.: Water vapour, sonoluminescence and sonochemistry. *Proc. R. Soc. Lond. A* **456**(1999), 1685 (2000)
80. Kanthale, P., Ashokkumar, M., Grieser, F.: Sonoluminescence, sonochemistry (H_2O_2 yield) and bubble dynamics: frequency and power effects. *Ultrason. Sonochem.* **15**(2), 143 (2008)
81. Mettin, R., Cairós, C., Troia, A.: Sonochemistry and bubble dynamics. *Ultrason. Sonochem.* **25**, 24 (2015)
82. Cavaliere, F., Chemat, F., Okitsu, K., Sambandam, A., Yasui, K., Zisu, B.: *Handbook of Ultrasonics and Sonochemistry*, 1st edn. Springer, New York (2016)
83. Hegedűs, F., Krähling, P., Aron, M., Lauterborn, W., Mettin, R., Parlitz, U.: Feedforward attractor targeting for non-linear oscillators using a dual-frequency driving technique. *Chaos* **30**(7), 073123 (2020)
84. Toda, M.: *Theory of Nonlinear Lattices*, 2nd edn. Springer-Verlag, New York (1989)
85. Scheffczyk, C., Parlitz, U., Kurz, T., Knop, W., Lauterborn, W.: Comparison of bifurcation structures of driven dissipative nonlinear oscillators. *Phys. Rev. A* **43**(12), 6495 (1991)
86. Kovacic, I., Brennan, M.J.: *The Duffing Equation: Nonlinear Oscillators and their Behaviour*. John Wiley & Sons, Hoboken (2011)
87. Cirillo, G.I., Habib, G., Kerschen, G., Sepulchre, R.: Analysis and design of nonlinear resonances via singularity theory. *J. Sound Vib.* **392**, 295 (2017)
88. Parlitz, U., Lauterborn, W.: Resonances and torsion numbers of driven dissipative nonlinear oscillators. *Z. Naturforsch. A* **41**(4), 605 (1986)
89. Lauterborn, W., Parlitz, U.: Methods of chaos physics and their application to acoustics. *J. Acoust. Soc. Am.* **84**(6), 1975 (1988)
90. Parlitz, U., Englisch, V., Scheffczyk, C., Lauterborn, W.: Bifurcation structure of bubble oscillators. *J. Acoust. Soc. Am.* **88**(2), 1061 (1990)
91. Englisch, V., Parlitz, U., Lauterborn, W.: Comparison of winding-number sequences for symmetric and asymmetric oscillatory systems. *Phys. Rev. E* **92**(2), 022907 (2015)
92. Lauterborn, W., Holzfuss, J.: Acoustic chaos. *Int. J. Bifurc. Chaos* **01**(01), 13 (1991)

Publisher's Note Springer Nature remains neutral with regard to jurisdictional claims in published maps and institutional affiliations.